Nanoscale

Accepted Manuscript

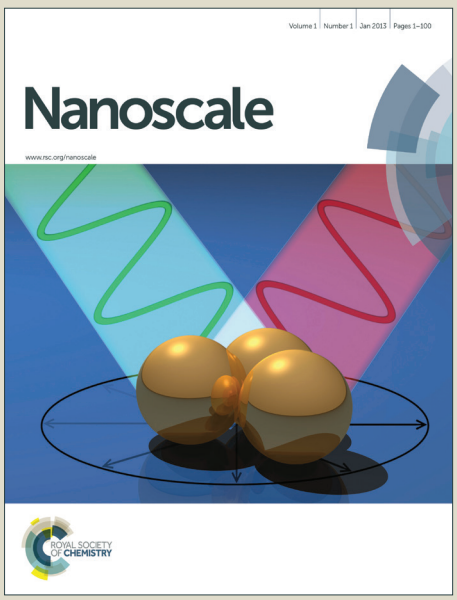

ROYAL SOCIETY OF CHEMISTRY

www.rsc.org/nanoscale

Journal Name

RSCPublishing

ARTICLE

LaF_3:Ln mesoporous spheres: controllable synthesis, tunable luminescence and application for dual-modal chemo-/photo-thermal therapy

Cite this: DOI: 10.1039/x0xx00000x

Received 00th January 2012,
Accepted 00th January 2012

DOI: 10.1039/x0xx00000x

www.rsc.org/

Ruichan Lv, Guixin Yang, Fei He*, Yunlu Dai, Shili Gai, and Piaoping Yang*

In this report, uniform LaF_3:Ln mesoporous spheres have been synthesized by a facile and mild *in situ* ion-exchange method using yolk-like $La(OH)_3$:Ln mesoporous spheres as template, which were prepared through a self-produced bubble-template route. It was found that the structures of the final LaF_3:Ln can simply be tuned by adding polyetherimide (PEI) reagent. LaF_3:Ln hollow mesoporous spheres (HMSs) and LaF_3:Ln flower-like mesoporous spheres (FMSs) were obtained when assisted by PEI and in the absence of PEI. The up-conversion (UC) luminescence results reveal that the doping of Nd^{3+} ions in LaF_3:Ln can markedly influence the UC emissions of the products. It is interesting that an obvious thermal effect is achieved due to the energy back-transfer from Tm^{3+} to Nd^{3+} ions under 980 nm near-infrared (NIR) irradiation. The LaF_3:Yb/Er/Tm/Nd HMSs shows good biocompatibility and sustained doxorubicin (DOX) release properties. In particular, upon 980 nm NIR irradiation, the photothermal effect arising from the Nd^{3+} doping induces a faster DOX release from the drug release system. Moreover, UC luminescence images of LaF_3:Yb/Er/Tm/Nd HMSs uptaken by MCF-7 cells exhibits apparent green emission under 980 nm NIR irradiation. Such multifunctional carrier combining UC luminescence and hyperthermia with the chemotherapeutic drugs should be highly potential for the simultaneous anti-cancer therapy and cell imaging.

1. Introduction

In modern material science and chemistry field, inorganic functional materials with special morphology have potential biomedical applications in the fields of drug delivery, disease diagnosis, and biological labeling.[1–5] Mesoporous materials have attracted wide attention due to the characteristic merits including large surface area, potential for high loading capacity, and low density.[6–8] Meanwhile, in the bio-imaging and drug carrier system, the lanthanide ion-doped nano-particles have been widely used because of their 4f electronic shells, relatively low toxicity, resistance to photo-bleaching, and UC emissions.[9–11] Specially, the NIR excitation at 980 nm is located within the optical transmission window of biological specimens, leading to deeper light penetration, decreased light scattering, decreased auto-fluorescence, increased image contrast, and decreased damage to cells.[12,13] The lanthanide fluoride, as the important up-conversion materials, which are one of the most widely used hosts to convert near-infrared photons via multi-photon processes into visible photons, has attracted wide attention.[14–18]

Considering these merits above, research has been focused on the direct assembly and fabrication of controlled functional structures which is not only of scientific interest but of down-to-earth practicality to the applied industry with such benefits as cost and energy savings. Silicate, carbonate, alkali, and alkaline-earth hybrid composites present advantages to design materials for hollow micro-/nano-photonic applications, which could be synthesized under low temperature and facile mild environment.[19–23] However, these materials could not be achieved as the desired UC luminescent hosts with high-efficiency and desired emission wavelength. Meanwhile, the conventional method could only get the simple structure of lanthanide fluoride.[24–28] Therefore, a route based on ion-exchange reactions has been regarded as an efficient way to obtain high-quality luminescent materials. This route is very attractive because it could duplicate the morphologies from the precursors with good morphology to final products. Although such route has been adopted to synthesize abundant materials, such as the metal and semiconductor,[29–35] it is still a challenge to synthesize lanthanide fluorides through the ion exchange method under mild facile condition.[36–38]

In the drug delivery systems (DDSs) , the key ability is to regulate drug release and improve therapeutic efficacy.[39] Various stimuli-sensitive biodegradable micelles that release drug in response to an internal or external stimulus like pH, reduction, and temperature have been developed to boost drug release.[40,41] Meanwhile, many researches have focused on the cation substitution in order to tune and optimize luminescent properties which may have other subsequent effects.[42–44] Most recently, Liu's group utilized the Nd^{3+} ions as the sensitizers for 800 nm excitation to improve the emission intensities associated with Yb^{3+} sensitization at 980 nm excitation.[45] Yan's group have used Nd^{3+} ions irradiated at 808 nm in order to minimize the laser-induced local overheating effect.[46] However,

for the drug carrier, the heating/photo-thermal effect caused by the energy-transfer process between different ions under lower pump power may have the benefit for the curative efficacy.[47] Meanwhile, NIR–NIR bio-imaging based on Nd^{3+} nanostructures has received interest because of its tissue safety and much higher signal-to-noise ratio.[48–50] Therefore, Nd^{3+} with Yb/Er, Yb/Ho, and Yb/Tm co-doped UC materials may generate the thermal effect and tune the luminescent emission regions under 980 nm NIR irradiation. As far as we know, there was few literature reported about the energy transfer process and the thermal effect of Nd^{3+} ions under 980 nm irradiation.

In this report, yolk-like $La(OH)_3$:Ln spheres were synthesized through a facile self-produced bubble-template process. After that, uniform LaF_3:Ln hollow mesoporous spheres and flower-like LaF_3:Ln mesoporous spheres were obtained using as-synthesized yolk-like $La(OH)_3$:Ln spheres as templates with and without PEI assistance before the fluorination process. UC emission intensities of different samples (the precursor, HMSs, and FMSs) were compared. Meanwhile, hemolysis assay and MTT assay experiment were employed to study the biocompatibility of the as-synthesized samples. Influence of the Nd^{3+} doping on the UC luminescence has been investigated. Furthermore, DOX loading and release, anti-cancer cytotoxicity, cellular uptake, and *in vitro* UC luminescence imaging of the as-synthesized products were also studied in detail. This mild, controllable, and high-producing method could be used to design other functional materials with ordered structure.

2. Experimental section

2.1. Chemicals and materials.

All of the chemical reagents used in this experiment are of analytical grade without any further purification, including nitric acid (HNO_3), citrate acid (H_3Cit), sodium hydroxide (NaOH), ethanol, sodium fluoroborate ($NaBF_4$) (Beijing Chemical Corporation), La_2O_3, Yb_2O_3, Er_2O_3, Ho_2O_3, Tm_2O_3, Nd_2O_3 (99.99%) (Sinopharm Chemical Reagent Co., Ltd.), PEI (Sigma-Aldrich), DOX, phosphate buffered saline (PBS), potassium hydrogen phthalate (PHP), folic acid (FA), 1-(3-dimethylaminopropyl)-3-ethylcarbodiimide hydrochloride (EDC), and N-hydroxysuccinimide (NHS) (Aladdin Chemical Reagent Co., Ltd.).

2.2. Synthesis

Synthesis of $La(OH)_3$:Ln HMSs. In a typical process, 0.5 M $La(NO_3)_3$ was prepared by dissolving corresponding La_2O_3 into HNO_3 with gradually heating. A total of 1 mL of 0.5 M $La(NO_3)_3$ and 1 mmol of citrate were added into 30 mL deionized water in a beaker. After stirred for 5 min, 10 mL aqueous solution containing 2.4 g NaOH was introduced to above reaction system and stirred for 10 min. Then the beaker was capped airtight and placed at 90 °C for 90 min through water bath without further stirring or shaking. The resulting precipitates were separated by centrifugation, washed with deionized water in sequence, and dried in air at 60 °C for 12 h, then $La(OH)_3$ hollow spheres were acquired. The preparation of $La(OH)_3$:Ln (Ln = Yb/Er, Yb/Tm, Yb/Tm/Nd, and Yb/Er/Tm/Nd) was similar to the above procedure.

Synthesis of LaF_3:Ln HMSs and FMSs. For the synthesis of LaF_3:Ln HMSs, the as-synthesized $La(OH)_3$:Ln HMSs were dispersed in 20 mL of water containing 0.1 g of PEI and stirred for 2 h. After that, 4 mmol of $NaBF_4$ was added with continuous stirring. After 10 min, the beaker was transferred to the water bath kettle at 90 °C. After reacting for 5 h, the resulted product was centrifuged for three times and dried for 12 h to obtain LaF_3:Ln HMSs. The LaF_3:Ln FMSs were synthesized in the similar process without adding PEI before the fluorination. For the targeted cell therapy, folic was conjugated on the surface of HMSs. 1 mg of FA, 2 mg of NHS and 6 mg of EDC were added into 20 mL of deionized water and stirred for 2 h in dark. After that, 20 mg of HMSs was added and reacted with stirring overnight at room temperature. The final LaF_3:Ln HMSs were recovered by centrifugation and washed twice with deionized water and ethanol to remove the free FA.

DOX loading and release test. 30 mg of LaF_3:Yb/Er/Tm/Nd HMSs samples was added into 5 mL of PBS and ultrasonically dispersed, respectively. After that, 2.5 mg of DOX was added into the solution with slow stirring at room temperature for 24 h. The as-synthesized mixture was centrifugally separated at 6000 rpm for 4 min, and then the supernatant solution was kept for ultraviolet visible light analysis. 10 mL of fresh PBS was replenished in the centrifugal tube during 8 hours, which was monitored by exposing the solution with or without 980 nm light irradiation. The process was repeated every one hour. The mass of the released DOX was obtained by the absorbance with the specified 480 nm.

***In vitro* viability.** 6000-7000 L929 fibroblast cells were plated in 200 mL media per well in a 96-well plate, then incubated 24 h to allow the cells to attach to the wells at 37 °C with 5% CO_2. The LaF_3:Yb/Er/Tm/Nd HMSs were sterilized *via* ultraviolet irradiation for 2 h, and then diluted at concentrations of 15.63, 31.25, 62.5, 125, 250, and 500 μg/mL, respectively. The solution with different concentration was added to the wells and incubated for another 24 h at 37 °C with 5% CO_2. Then 20 μL (5 mg/mL) of MTT solution was added to each well containing different amounts of HMSs. The plate was incubated at 37 °C for another 4 h subsequently. During this period, viable cells make MTT reduce into formazan which can be dissolved by DMSO. The absorbance of the suspension was recorded using a microplate reader regulating to 490 nm as detecting wavelength.

For the cytotoxicity of the LaF_3:Yb/Er/Tm/Nd HMSs, the process were similar to the viability with the HeLa cells instead. The NIR irradiation were carried on with pump power of 0.6 W/cm^2 for 5 min for one well. Trypan blue dyed experiment were carried out to assess the cytotoxicity of LaF_3:Yb/Er/Tm/Nd+DOX under NIR irradiation. Briefly, HeLa cells were incubated at 37 °C with 5% CO_2 to obtain monolayer cells in the media. After that, 1 mL of LaF_3:Yb/Er/Tm/Nd+DOX with culture were added to the media and incubated for another 6 h, and then irradiated under NIR laser. After that, 1 mL of trypan blue (0.4g/L) was added to mark dead cells.

Hemolysis assay. The red blood cells were obtained by removing the serum from the EDTA.K2 stabilized human blood through washing with 1% normal saline and centrifugation five times. After that, the blood cells were diluted to 1/10 with PBS solution (pH = 7.4). Diluted cells suspension (0.4 mL) was then mixed with: (1) PBS (1.6 mL) as a negative control; (2) deionized water (1.6 mL) as a positive control; (3) the materials suspensions (1.6 mL) with varying concentrations (15.63, 31.25, 62.5, 125, 250, 500 μg/mL). The ten samples were shaken and kept stable for 2 h at room temperature. Finally, the mixtures were centrifuged and the absorbance of the upper supernatants was measured by UV-vis characterization. The percentage of hemolysis was calculated using the following equation (A is the absorbance of UV-vis spectra): Hemolysis % = $(A_{sample} - A_{control(-)}) / (A_{control(+)} - A_{control(-)})$.

Cellular uptake. Cellular uptake by HeLa cancer cells was detected using a confocal laser scanning microscope (CLSM, Leica TCS SP8). HeLa cells were seeded in a 6-well culture plate and grown at 37 °C overnight. After that, the HeLa cells were incubated with LaF_3:Yb/Er/Tm/Nd+DOX at 37 °C for 0.5 h, 1 h, 3 h, and 6 h, respectively. Then, the cells were rinsed with PBS three times, and fixed with 2.5% formaldehyde (1 mL/well) at 37 °C for 10 min, and

rinsed again with PBS three times. The nuclei were dyed with DAPI solution (20 μg/mL in PBS, 1 mL/well) for 10 min for labeling the nucleus. After that, the cells were rinsed with PBS three times.

UC luminescence microscopy (UCLM) observation. UC luminescence imaging of MCF-7 cells (5×10^4/well) were seeded in 6-well culture plates and grown overnight. After that, these cells were incubated for different times (0.5 h, 1 h, 3 h, and 6 h) at 37 °C with LaF_3:Yb/Er/Tm/Nd HMSs. The cells were washed using PBS solution three times, and fixed with 1 mL of 2.5% formaldehyde in each well for 10 min. After that, the as-synthesized cells were washed with PBS three times.

2.3. Characterization.

Powder X-ray diffraction (XRD) measurements were performed on a Rigaku D/max TTR-III diffractometer at a scanning rate of 15°/min in the 2θ range from 10° to 80°, with graphite monochromatized Cu Kα radiation (λ = 0.15405 nm). Images were obtained digitally on scanning electron microscope (SEM, JSM-6480A), transmission electron microscopy (TEM, FEI Tecnai G^2 S-Twin) and high-resolution transmission electron microscopy (HRTEM). The compositions of the as-synthesized samples were equipped with an energy dispersive X-ray spectrum (EDS, JEOL JXA-840). Fourier transform IR (FT-IR) spectra were measured on a PerkinElmer 580B IR spectrophotometer using the KBr pellet technique. Nitrogen absorption/desorption isotherms were obtained at 77 K using a Micromeritics Tristar 3020 instrument. The specific surface area was calculated by the Brunauer-Emmett-Teller (BET) method. The pore size distribution was measured using the Barret-Joner-Halenda (BJH) method. UC emission spectra were obtained using 980 nm LD Module (K98D08M-30W, China) as the excitation source and detected by R955 (HAMAMATSU). All the UC spectra in our experiment were gained under 980 nm laser diode with the same signal amplification. DOX concentration was detected by UV-1601 spectrophotometer. The measurements were wholly performed at room temperature.

3. Results and discussion

3.1. Phase, structure, and morphology

The formation of LaF_3:Ln HMSs and LaF_3:Ln FMSs can be illustrated as Scheme 1. It is well known that the low doping concentration of rare earth ions (0.5%Er, 0.5%Tm, 1%Nd) has little influence on the phase or shape of the final product due to their much similar ionic radius, so here Ln doped sample is taken as the typical example to elucidate the phase, structure, and shape of the doped products. Fig. 1A shows XRD patterns of the $La(OH)_3$:Ln precursor, LaF_3:Ln HMSs and LaF_3:Ln FMSs. On the basis of the Joint

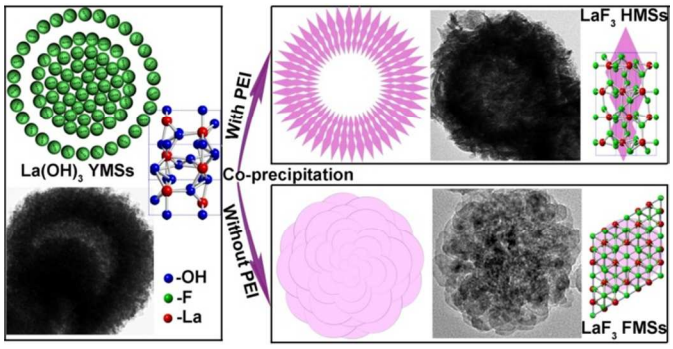

Scheme 1 Illustration for the morphology evolution of LaF_3:Ln with hollow and flower-like structures.

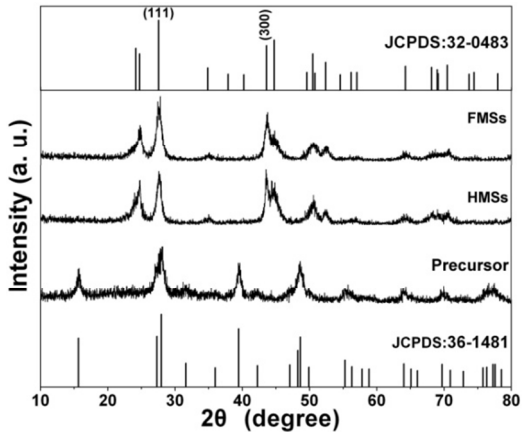

Fig. 1 XRD patterns of as-synthesized $La(OH)_3$:Ln precursor, LaF_3:Ln HMSs and LaF_3:Ln FMSs.

Committee on Power Diffraction Standard (JCPDS) reference database, the diffraction peaks of the precursor are well indexed to hexagonal $La(OH)_3$ (JCPDS No. 36–1481). Also, the diffraction peaks of the resulting LaF_3:Ln HMSs and FMSs can well coincide with hexagonal-phased LaF_3 (JCPDS No. 32–0483). Meanwhile, the wide diffraction peaks imply nano-size nature of the as-synthesized samples. The average crystalite sizes can be calculated from theS cherrer formula: $D_{hkl} = K\lambda/(\beta\cos\theta)$, where K is a constant of 0.89, θ is the diffraction angle, β is the full-width at half-maximum. The calculated crystallite sizes of $La(OH)_3$:Ln precursor, the as-synthesized LaF_3:Ln HMSs and LaF_3:Ln FMSs are 7.9 nm, 10.3 nm and 9.6 nm, respectively.

The morphology of as-synthesized $La(OH)_3$:Ln precursor is given in Fig. 2A-C. As shown, obvious yolk-like structure can be obtained evidenced by the dark core and shell, with the clear

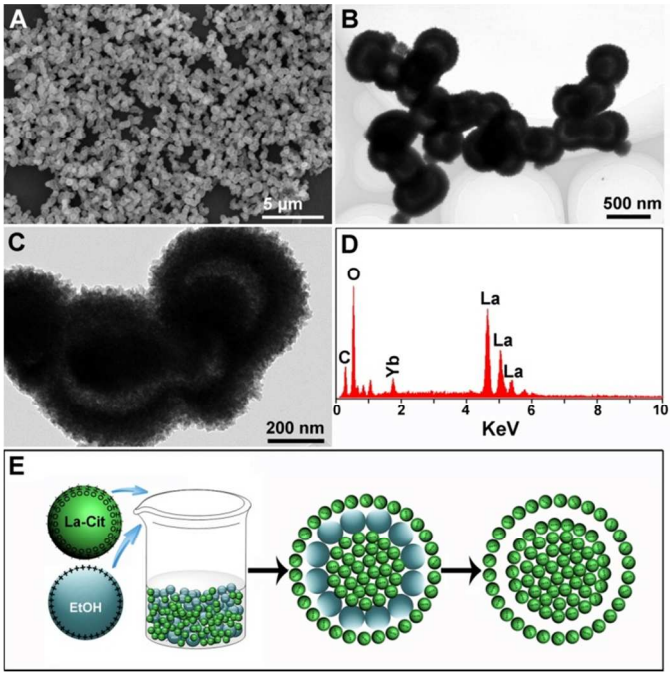

Fig. 2 (A) Structural characterization of the as-synthesized $La(OH)_3$:Ln precursor. (B, C) SEM image, TEM images with different magnification, (D) EDS pattern, and (E) the formation scheme of the yolk-like $La(OH)_3$:Ln spheres.

hollow space between the core and shell. EDS pattern in Fig. 2D confirms the presence of La, Yb, C, and O elements in the sample. The C element is due to the survived citric acid ions and conductive adhesive. The formation scheme of $La(OH)_3$:Ln precursor is proposed in Fig. 2E. Citric acid has widely been used to control the morphology of the product as one of commonly used surfactants. Here, H_3Cit plays the key role in forming the Ln-Cit complex. Meanwhile, the ethanol bubbles are generated due to the super-saturation of the solution under the temperature of 90 °C. The bubbles separate the quickly formed $La(OH)_3$ nanospheres and the nanospheres are attached on the surface of the bubbles due to the electrostatic effect. After the co-precipitation process, the yolk-like structure is acquired.

When PEI is added before the fluorination process, LaF_3:Ln hollow spheres were obtained. TEM images in Fig. 3A-C indicate that these hollow spheres are uniform with an average size of 300 nm. The selected area electron diffraction (SAED) pattern of a single hollow sphere (inset in Fig. 3B) manifests as a regular array of diffraction spots along the (111) and (300) planes, which is consistent with the two main diffractions in the XRD pattern of LaF_3:Ln HMSs. In the HRTEM image (Fig. 3D), lattice fringes with the same interspacing of 0.32 nm can be seen clearly, corresponding to the (111) planes of typical hexagonal LaF_3 crystal.[51] The (300) plane with the interspacing of 0.22 nm can be also observed, which is well consistent with the XRD and SAED patterns. EDS pattern (Fig. 3E) indicates the presence of La, Yb, and F elements in the LaF_3:Ln sample. No O element can be detected, indicating the complete transfer from $La(OH)_3$:Ln to LaF_3:Ln.

When there is no PEI added before the fluorination process, the flower-like LaF_3:Ln is obtained. A panoramic view (Fig. 4A) reveals that the sample entirely consists of uniform flower-like spheres without aggregation. The average size of the flower-like spheres is 180 nm. SAED pattern (inset in Fig. 4B) and the diffraction loops with corresponding lattice planes (Fig. S1) are presented. The typical (110), (111), (300), (220), and (330) lattice planes are consistent with the XRD pattern of single-crystal hexagonal LaF_3. In Fig. 4C, the FMSs are composited with nano-flakes and overlapped to form the flower (inset in Fig. 4C). The size of follower-like LaF_3:Ln is much smaller than that of hollow LaF_3:Ln which is attributed to the absence of PEI. The HRTEM image (Fig. 4E) with a single nanocrystal

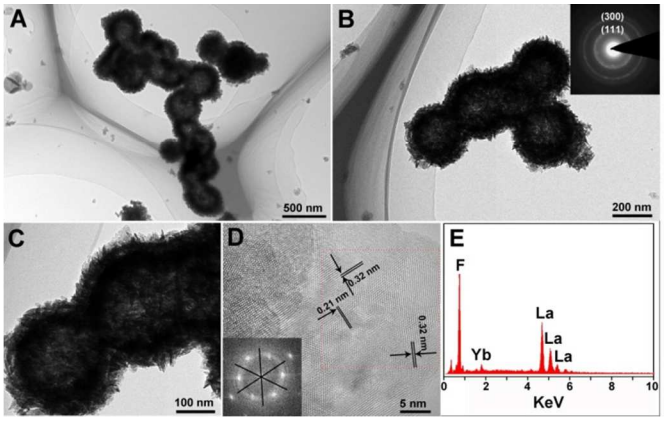

Fig. 3 Structural characterization of LaF_3:Ln HMSs. (A-C) TEM images with different magnification, HRTEM image and (D) the corresponding FFT pattern, and (E) EDS pattern of LaF_3:Ln HMSs. Inset in panel B is the corresponding SAED pattern of LaF_3:Ln hollow spheres.

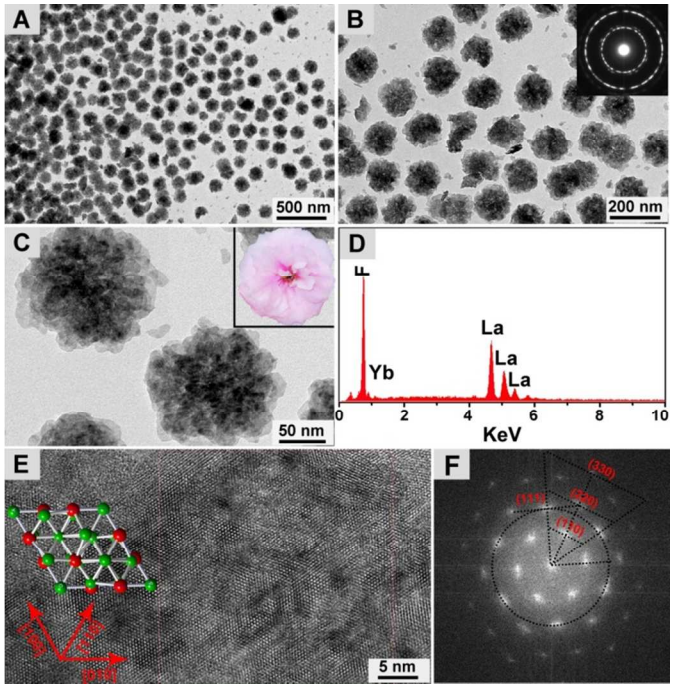

Fig. 4 Structural characterization of LaF_3:Ln FMSs. (A-C) TEM images with different magnification, (inset of B) the corresponding SAED pattern and (inset of C) the cherry blossom photograph, (D) EDS pattern, (E) HRTEM image and (F) the corresponding FFT pattern with a single nanocrystal taken in (100) direction.

taken in (001) crystal face clearly shows that the composited crystal is hexagonal. The corresponding FFT pattern (Fig. 4F) presents that the respective distance of (110), (220), and (330) planes is 0.36 nm, 0.18 nm, and 0.12 nm. According to the calculation formula: $1/d^2 = h^2/a^2 + k^2/b^2 + l^2/c^2$ (h, k, and l mean the crystal indices), the calculated ratio of the three planes is 3:2:1. No other crystal plane appears in Fig. 4F, which further confirms the crystalline purity of the FMSs.

Above XRD results indicate that both $La(OH)_3$:Ln and LaF_3:Ln are hexagonal phases. Fig. 5A and 5B give the respective crystal structure of $La(OH)_3$ and LaF_3 taken from the crystal face of (010) and (001). It can be identified that the framework structures of two compounds are almost identical except that the OH^- ions are substituted by the F^- ions *in situ*. When PEI was added, the PEI protects the precursor inside, which inhibits the LaF_3 crystals growing in all directions. Consequently, $La(OH)_3$ crystals slowly transfer to LaF_3 crystals which promote the hexagonal growth along z axis, keeping their direction along [001] direction (Fig. 5C1). Hollow LaF_3

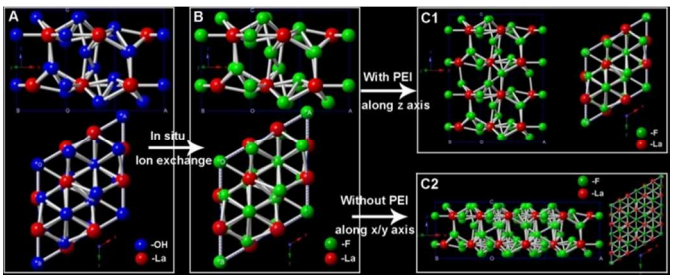

Fig. 5 (A) Crystal structure of hexagonal $La(OH)_3$, (B) hexagonal LaF_3, (C1) the generated HMSs and (C2) FMSs.

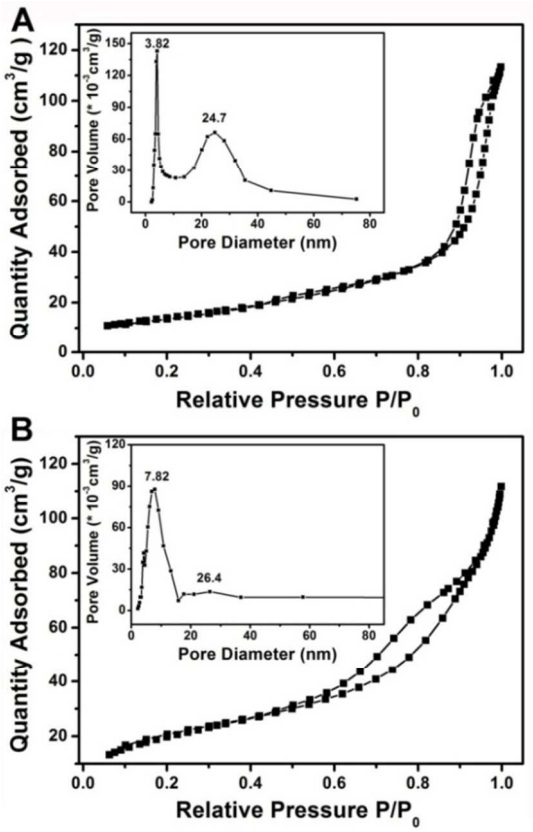

Fig. 6 Nitrogen adsorption/desorption isotherms of (A) LaF_3:Ln HMSs and (B) LaF_3:Ln FMSs. Insets are their corresponding pore size distribution curves.

spheres are formed by *in situ* ion-exchange because of the slow growth rate of LaF_3 and fast dissolution rate of $La(OH)_3$. When there is no PEI added, LaF_3 crystals generate and grow fast without inhibition. Consequently, $La(OH)_3$ dissolves fast and the generated LaF_3 grows to nanoflakes along the x/y axis which is the (001) lattice plane (Fig. 5C2). After that, the nano-flake crystal was formed to flower-like spheres.

FT-IR spectra of the $La(OH)_3$:Yb/Er precursor, LaF_3:Yb/Er HMSs and LaF_3:Yb/Er FMSs are given in Fig. S2. It is found that similar bands in all three samples at 3431 cm^{-1}, 1082 cm^{-1}, and 650 cm^{-1} are due to the -OH stretching and bending vibrations of water and hydroxyl groups, respectively.[52] For the precursor, the peaks at between 1400 cm^{-1} and 1600 cm^{-1} arise from the (C=O) stretching mode, which may be ascribed to the addition of Cit^{3-} ions in the hydrothermal process.[53] Compared with FMSs, HMSs have several characteristic absorptions of PEI at 2928 cm^{-1}, 1420 cm^{-1}, and 780 cm^{-1}, which can be assigned to the -CH asymmetric stretching vibration, -CN stretching vibrations, and -NH stretching vibration in the carboxyl group, respectively.[54] FT-IR result demonstrates that we have succeeded modified PEI on the surface of the precursor before generating HMSs.

N_2 adsorption/desorption isotherms and corresponding pore size distributions of LaF_3:Ln HMSs and LaF_3:Ln FMSs are shown in Fig. 6, respectively. It can be seen that both samples exhibit typical IV-type isotherms with H_1 hysteresis loops, indicating the mesoporous nature. The BET surface area, total pore volume, and average pore width of LaF_3:Yb/Er HMSs are calculated to be 50.2 m^2/g, 0.175 cm^3/g, and 13.8 nm, respectively. And the corresponding values of LaF_3:Ln FMSs are calculated to be 75.2 m^2/g, 0.179 cm^3/g, and 9.41 nm, respectively. For LaF_3:Ln HMSs, the presence of pores in the shell and the hollow interior structure may result in the two different pore sizes distribution, locating at 3.82 nm and 24.7 nm, respectively. For LaF_3:Ln FMSs, the wide pore size distribution at 7.82 nm and 26.4 nm should be due to the different distances between the layers of the flakes from inside to outside.

3.2. Photoluminescence properties.

In order to evaluate the luminescent properties of the samples with different structures, we detected the UC emission spectra of the precursor, LaF_3:10%Yb/1%Er (Ho, Tm) of the HMSs and FMSs under 980 nm NIR laser excitation, as shown in Fig. S3. It is obvious that the precursor has no emission peaks. The emission spectra of both LaF_3:Yb/Er structures contain three chief emission peaks at 523, 549, and 661 nm, corresponding to the respective $^2H_{11/2} \rightarrow {}^4I_{15/2}$, $^4S_{3/2} \rightarrow {}^4I_{15/2}$, and $^4F_{9/2} \rightarrow {}^4I_{15/2}$ transition of Er^{3+}.[55,56] FMSs have higher intensity than that of HMSs, which may be due to more surface defect caused by the hollow structure. The emission spectra of Yb/Tm (Fig. S3B) and Yb/Ho (Fig. S3C) co-doped $La(OH)_3$, LaF_3 HMSs and FMSs have the similar results to those of Yb/Er co-doped samples. No emission peak appear in the $La(OH)_3$:Yb/Ho and $La(OH)_3$:Yb/Tm samples. The emission intensities of LaF_3:Yb/Ho and LaF_3:Yb/Tm FMSs are higher than those of HMSs, respectively. It is known that the intensity of the UC phosphors is influenced by many factors, such as size, shape, structure, and defect. Although the size of FMSs is smaller than

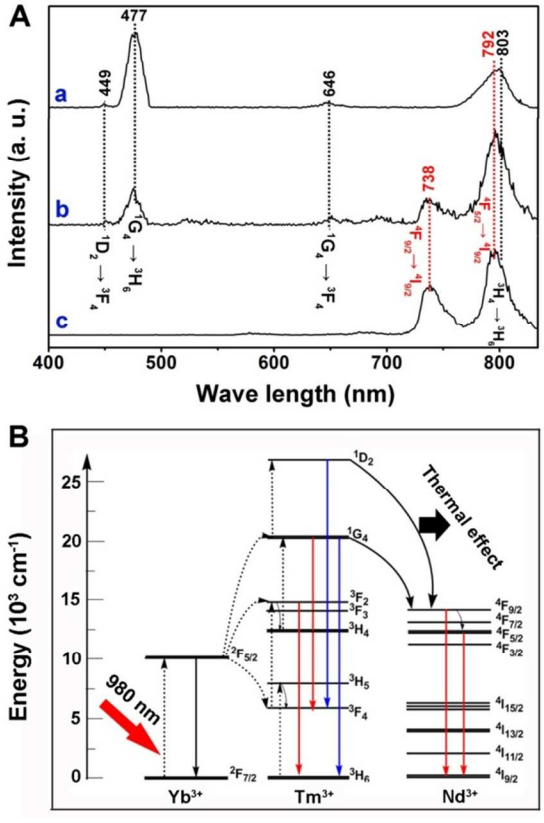

Fig. 7 (A) UC emission spectra of (a) LaF_3:10%Yb/0.5%Tm, (b) LaF_3:10%Yb/0.5%Tm/1%Nd, (c) LaF_3:10%Yb/0.5%Tm/2%Nd HMSs; (B) the proposed energy transfer mechanism using the energy level diagram under 980 nm excitation with the pump power of 0.6 W/cm^2.

that of HMSs, the structure of FMSs and HMSs are much different. As shown in Fig. 3 and 4, LaF_3:Ln HMSs is hollow with more surface defect, and the LaF_3:Ln FMSs is flower-like with less surface defect. Thus, the FMSs may have higher UC emission intensity than that of HMSs. In a sum, this *in situ* ion-exchange method can be well used to synthesize functional materials with tuned luminescence.

Most recently, Yao's group designed a transition layer into core-shell structure to fabricate a quenching-shield which blocks the energy back-transfer from activators to the sensitizer Nd^{3+}.[57] In another side, if the "quenching" is optimized to the appropriate extent, they may have the comprehensive properties for both luminescent and biological application. Thus, we prepared LaF_3:10%Yb/0.5%Tm/x%Nd (x = 0, 1, and 2) with different Nd^{3+} doping, and the UC emission spectra under 980 nm NIR excitation are given in Fig. 7A. Note that we choose HMSs rather than FMSs. Firstly, both of the two samples have high BET surface which is beneficial to adsorb large amount of drug molecules. However, compared with FMSs, the HMSs has a large cavity which can store more drug molecules than that of FMSs. Secondly, when the composite is under the release environment, the initial fast release and the following modest release are needed. The HMSs have a special small pore distribution which is favourable to generate a slow release process. The black and red dotted lines correspond to the energy transitions of Tm^{3+} ions and Nd^{3+} ions, respectively. The four emission peaks at 449, 477, 646, and 803 nm are ascribed to the $^1D_2 \rightarrow {}^3F_4$, $^1G_4 \rightarrow {}^3H_6$, $^1G_4 \rightarrow {}^3F_4$, and $^3H_4 \rightarrow {}^3H_6$ transition of Tm^{3+}.[58–60] The red emissions at 738 nm and 792 nm are assigned to the $^4F_{9/2} \rightarrow {}^4I_{9/2}$ and $^4F_{5/2} \rightarrow {}^4I_{9/2}$ transitions of Nd^{3+} ions. For Yb/Tm co-doped LaF_3, the blue emissions are more intense than the red and NIR up-conversion emissions. When the Nd^{3+} concentration is increased from 1% to 2%, the blue emissions decrease markedly and almost disappear, and the red/NIR emissions increase obviously. Fig. S4 presents the corresponding CIE chromaticity diagram of LaF_3:10%Yb/0.5%Tm/x%Nd (x = 0, 1, and 2) under 980 nm NIR excitation. The coordinates of the three samples are (0.151, 0.121), (0.205, 0.224), (0.478, 0.411), respectively. It shows the luminescent color changes from purple to orange with the increase of Nd^{3+} concentration. The decrease of the UC emission is due to the energy back-transfer from Tm^{3+} ions to Nd^{3+} ions.[61] In another side, LaF_3:10%Yb/0.5%Tm/2%Nd nearly presents a single-red-region UC luminescent property. In comparison with multicolor UC materials, the single-red-region UC material is more preferable to serving as ideal optical bio-labels for deep-tissue imaging *in vivo*, since the red emission falls within the "optical window" of the biological tissues, which can afford deep tissue penetration.[62] However, for comprehensive consideration of avoiding the luminescence quenching and ensuring the thermal effect, we chose 1% as the optimized doping concentration of Nd^{3+} ions. The energy transfer of $Yb^{3+}/Tm^{3+}/Nd^{3+}$ ions is presented by the energy level diagram (Fig. 7B). The photons on the $^1D_2$ and $^1G_4$ levels of Tm^{3+} ions are transferred to $^4F_{5/2}$ level of Nd^{3+} ions, which may introduce the thermal effect and tune the UC emission.

3.3 Drug release, *in vitro* viability, cellular uptake and bioimaging

Considering the maintenance of UC luminescence and thermal effect arising from doping Nd^{3+}, we prepared the LaF_3:10%Yb/0.5%Er/0.5%Tm/1%Nd HMSs as the final multi-functional material. The UC emission spectrum of the sample under 980 nm NIR excitation is given in Fig. 8A. We can see

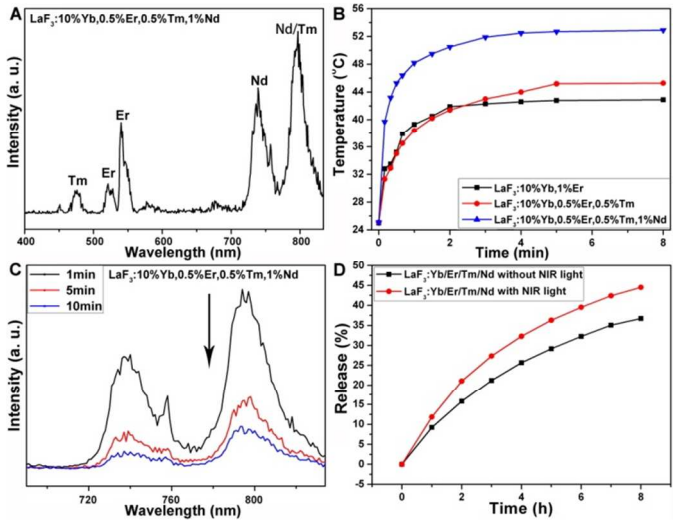

Fig. 8 (A) UC emission spectrum of LaF_3:10%Yb/0.5%Er/0.5%Tm/1%Nd HMSs; (B) the temperature as function of the laser irradiated time for LaF_3:10%Yb/1%Er, LaF_3:10%Yb/0.5%Er/0.5%Tm, and LaF_3:10%Yb/0.5%Er/0.5%Tm/1%Nd; (C) the UC emission spectra of LaF_3:10%Yb/0.5%Er/0.5%Tm/1%Nd HMSs irradiated with different time, and (D) DOX release efficiencies of LaF_3:10%Yb/0.5%Er/0.5%Tm/1%Nd HMSs with and without 980 nm laser irradiation. The spectra were all detected with the pump power of 0.6 W/cm^2.

the characteristic peaks are assigned to Er^{3+}, Tm^{3+}, and Nd^{3+} ions. The corresponding CIE coordinates are determined to as x = 0.261, y = 0.552, locating in the green region (Fig. S5). The temperatures of different samples (LaF_3:10%Yb/1%Er, LaF_3:10%Yb/0.5%Er/0.5Tm, and LaF_3:10%Yb/0.5%Er/0.5%Tm/1%Nd) as a function of the irradiation time under 980 nm laser irradiation were detected and recorded by the infrared thermal images (Fig. 8B and Fig. S6). It is obvious that the temperature of LaF_3:10%Yb/0.5%Er/0.5%Tm/1%Nd is much higher than those of the samples without Nd^{3+} doping, which is due to the non-radiative transitions. In Fig. S6, the infrared thermal images directly show the strong thermal effect of LaF_3:10%Yb/0.5%Er/0.5%Tm/1%Nd. Fig. 8C shows the emission spectra of LaF_3:Yb/Er/Tm/Nd irradiated with different time. It is found that the emission intensity decreases with the irradiation time, which should be due to the thermal quenching effect. The results indicate LaF_3:Yb/Er/Tm/Nd HMSs are potential candidate as the light-triggered drug carrier due to the thermal effect.

In order to further utilize the thermal effect of LaF_3:Yb/Er/Tm/Nd HMSs under 980 nm NIR laser which would be an "on/off" pattern to control the release process, the release efficiencies of DOX loaded LaF_3:Yb/Er/Tm/Nd HMSs with and without the NIR light excitation were monitored. Fig. 8D shows that the release efficiency with the NIR laser irradiation is up to 1.2-1.4 times compared with that without laser irradiation. The result reveals that the dose of the released drug can be regulated by controlling the sample exposed to laser or not. The initial rapid release of DOX molecules is essential to cure tumor cells, and the slow release of rest drug molecules can be continued for curbing the survived cells.

Standard MTT cell assay was performed on L929 cell lines to test the viability of LaF_3:Yb/Er/Tm/Nd HMSs. Fig. 9Ashows the cell viability with different concentration of the sample varying from 15.63 to 500 ug/mL incubated for 24 h. It is found that the cell viability of the sample in all dosages is up to 89.9%–105.5%. There is still 89.9% found even at a high dose

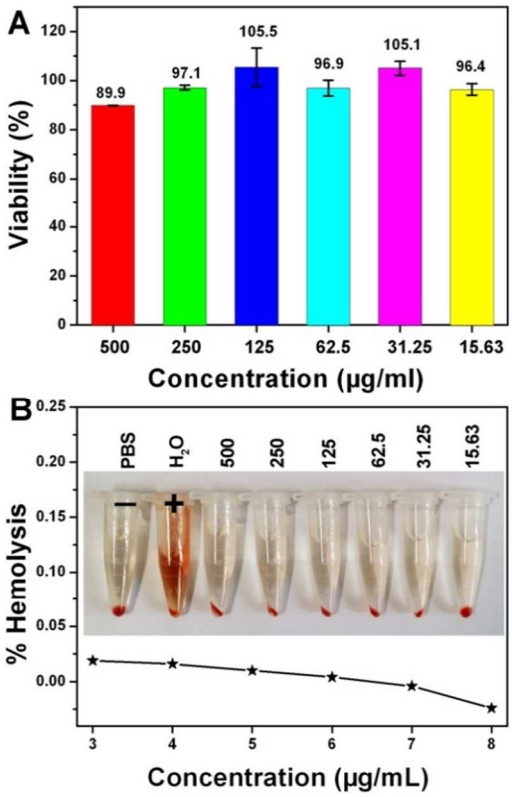

Fig. 9 (A) Cell viability of LaF_3:Yb/Er/Tm/Nd HMSs incubated with L929 cells and (B) hemolysis percentage of LaF_3:Yb/Er/Tm/Nd HMSs to human red blood.

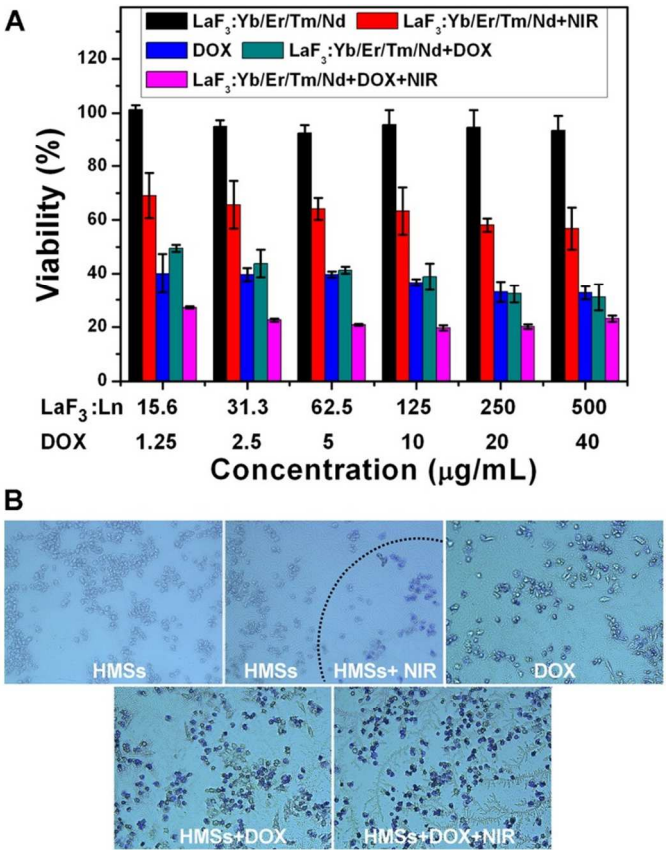

Fig. 10 (A) *In vitro* viability of HeLa cells incubated for 24 h with DOX, HMSs, HMSs+DOX at varied concentration with and without NIR-laser irradiation; (B) HeLa cells dyed with trypan blue treated with different groups.

concentration of 500 μg/mL. The result reveals that LaF_3:Yb/Er/Tm/Nd HMSs have high cell compatibility and low toxicity. Moreover, it is important to detect the biocompatibility of the sample with blood cells to guarantee the successful intravenous administration as the anticancer chemotherapy, as shown in Fig. 9B. During the hemolysis assay process, the obtained red solution dissolved with H_2O is due to the hemoglobin released into the solution. While for the controlled tubes with the PBS and the sample with different solution added, there is no obvious visually red occurred, indicating there is no or negligible hemolysis. The highest hemolytic efficiency with different materials concentration from 15.63 to 500 μg/mL is 0.02% which indicates the LaF_3:Yb/Er/Tm/Nd HMSs is almost no hemolytic. Thus, it is inferred the blood compatibility of the as-synthesized product is excellent.

Standard MTT cell assay incubated with HeLa cells were carried out in order to detect the cytotoxicity of LaF_3:Yb/Er/Tm/Nd HMSs loaded with DOX. Fig. 10 presents the cell viability with different concentration of HMSs varying from 15.63 to 500 μg/mL (corresponding to the concentration of loaded or free DOX from 1.25 to 40 μg/mL) incubated with HeLa cells for 24 h. It is obvious that the pure material is non-toxic with the viability of 92.6%-101.3%. When there is NIR irradiation with the pure material, the cancer cell viability is decreased to 56.7%-69.0% which may be due to the thermal effect. For the free DOX and the sample loaded with DOX, the viability is similar with an obvious inhibition to the cells. In particular, when there is NIR irradiation, the viability of the cancer cells (19.6%-27.2%) is much lower than those of all above. IC_{50} value of the LaF_3:Yb/Er/Tm/Nd+DOX+NIR is 1.05 μg/mL, which is smaller than that of the pure DOX with a value of 3.25 μg/mL. As shown in Fig. 10B1, B2, the cells incubated with HMSs in the regions without NIR are still survived, while the cells in the regions with NIR are killed mostly. Meanwhile, the cells incubated with DOX and HMSs+DOX are killed partly. When there is NIR irradiated, cells incubated with HMSs+DOX are killed mostly. The trypan blue results are well consistent with MTT assay. The result further reveals that the as-synthesized sample has the light-triggered thermal effect which makes the sample reach the simultaneous chemo- and photothermal- therapy.

The CLSM photographs of HeLa cancer cells incubated with LaF_3:Yb/Er/Tm/Nd+DOX HMSs for 0.5 h, 1 h, 3 h, and 6 h at 37 °C were taken to verify the cell uptake process, as shown in Fig. 11. Each group can be classified into the nuclei of cells dyed by DAPI (DAPI marked by green color for better distinguishability), the red emission caused by DOX, and an overlay of the both channels, respectively. It is found that in the first 0.5 h, little red emission is detected which indicates only a few LaF_3:Yb/Er/Tm/Nd+DOX HMSs are taken up by cells. Strong red fluorescence of DOX is observed in both the cytoplasm and the cell nucleus with the increased incubation time, revealing more particles cross the membrane and are localized in the cytoplasm. The results indicate that the as-synthesized HMSs can be effectively taken up by cancer cells.

Fig. 12 gives the inverted florescence microscope images of MCF-7 cells incubated with LaF_3:Yb/Er/Tm/Nd HMSs for 0.5 h, 1 h, 3 h, and 6 h at 37 °C, which were measured by a confocal microscope equipped with a 980 nm NIR laser.[63] In Fig. 12A2-D2 and A3-D3, the UC luminescent signal at red and

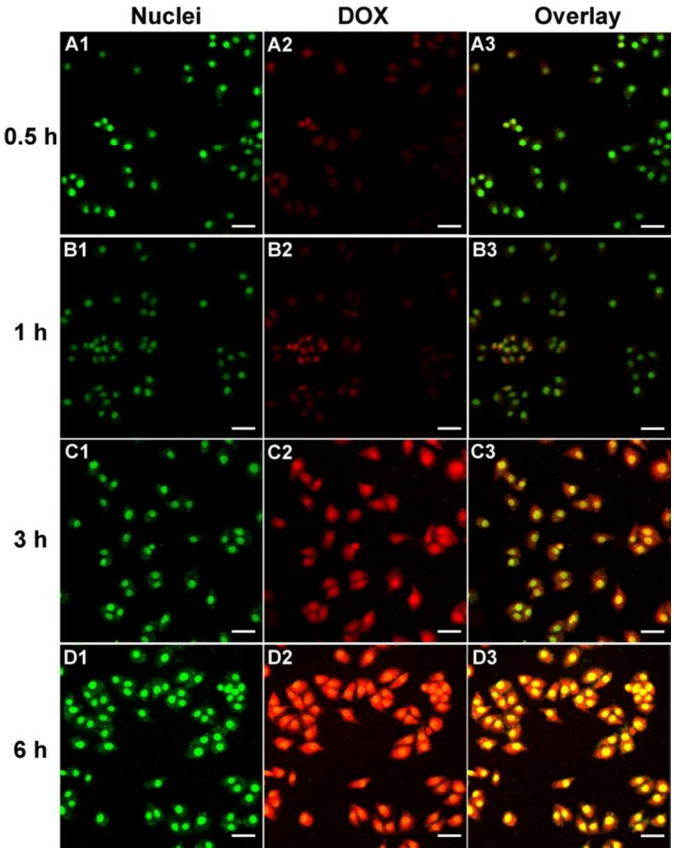

Fig. 11 Confocal laser scanning microscopy (CLSM) images of HeLa cancer cells incubated with LaF_3:Yb/Er/Tm/Nd+DOX for (A1-A3) 30 min, (B1-B3) 1 h, (C1-C3) 3 h, and (D1-D3) 6 h at 37 °C. Scale bars for all images are 50 μm.

green region is detected. Bright-field (Fig. 12A1-D1) and overlays (Fig. 12A4-D4) of confocal luminescence images are also presented. The UC luminescence emission of LaF_3:Yb/Er/Tm/Nd HMSs is increased with the enhanced time. Meanwhile, the luminescence is evident in the intracellular region while no signal outside of cells is found ,which further proves that the HMSs have been internalized into the cells rather than merely staining the membrane surface. The results demonstrate that the as-synthesized LaF_3:Yb/Er/Tm/Nd HMSs are promising candidates for high-contrast *in vitro* bio-imaging with negligible background.

Conclusions

In summary, yolk-like $La(OH)_3$:Ln mesoporous spheres were firstly synthesized by a bubble-template co-precipitation process. After that, the uniform hollow and flower-like LaF_3:Ln mesoporous spheres were synthesized in situ by the ion exchange of $NaBF_4$ with and without PEI added. This in situ ion-exchanged method under mild conditions without further calcination can be well used to design highly efficient luminescent materials with complex but ordered structure. Meanwhile, with Nd^{3+} ions co-doped, the UC luminescent properties are tuned with red emissions increased and the thermal effect is due to the energy transfer from Tm^{3+} to Nd^{3+} ions. The Yb/Er/Tm/Nd co-doped LaF_3 HMSs would be candidate as the multi-functional (mesoporous, UC luminescent, NIR light-triggered release, dual-modal chemo- and photothermal-therapy) material.

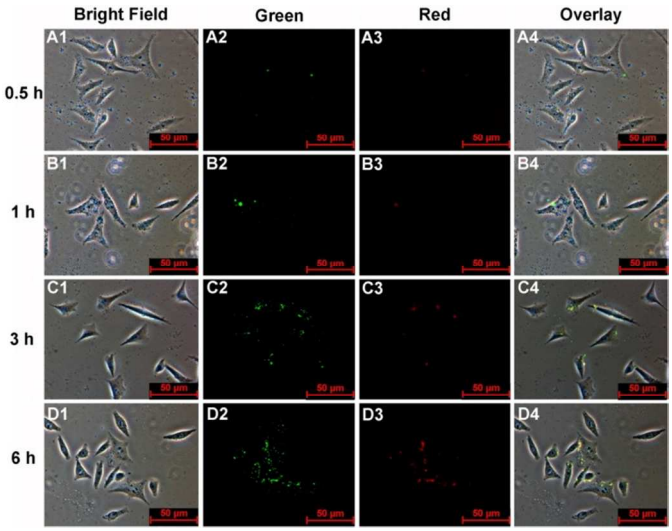

Fig. 12 Inverted fluorescence microscope images of MCF-7 cells incubated with LaF_3:Yb/Er/Tm/Nd HMSs for (A1–A3) 0.5 h, (B1–B3) 1 h, (C1–C3) 3 h, and (D1–D3) 6 h.

Acknowledgements

This work was supported by funding from financial supports from the National Natural Science Foundation of China (NSFC 21271053, 21401032, 51472058), Research Fund for the Doctoral Program of Higher Education of China (2011230411002), Natural Science Foundation of Heilongjiang Province (B201403), Program for New Century Excellent Talents in University, Harbin Sci.-Tech. Innovation Foundation (RC2012XK017012, 2014RFQXJ019) and Fundamental Research Funds for the Central Universities of China (HEUCF201403006).

Notes and references

Key Laboratory of Superlight Materials and Surface Technology, Ministry of Education, College of Material Science and Chemical Engineering, Harbin Engineering University, Harbin 150001, P. R. China. E-mail: yangpiaoping@hrbeu.edu.cn; hefei1@hrbeu.edu.cn

† Electronic Supplementary Information (ESI) available: [SAED pattern of flower-like LaF_3:Yb,Er spheres. FT-IR spectra of the $La(OH)_3$:Ln precursor, LaF_3:Ln HMSs and LaF_3:Ln FMSs. UC emission spectra of the $La(OH)_3$:Yb/Er(Ho/Tm) precursor, LaF_3:Yb/Er(Ho/Tm) HMSs, LaF_3:Yb/Er(Ho/Tm) FMSs under 980 nm NIR excitation. CIE chromaticity diagram of LaF_3:10%Yb/0.5%Tm/x%Nd (x = 0, 1, 2) under 980-nm NIR excitation. CIE chromaticity diagram of LaF_3:Yb/Er/Tm/Nd under 980 nm NIR excitation. Infrared thermal image of LaF_3:Yb/Er, LaF_3:Yb/Er/Tm, and LaF_3:Yb/Er/Tm/Nd sample before and after irradiated for 6-8 min under 980 nm laser irradiation with the pump power of 0.6 W/cm^2.]. See DOI: 10.1039/b000000x/

1 P. A. Ma, H. Xiao, X. Li, C. Li, Y. Dai, Z. Cheng, X. Jing and J. Lin, *Adv. Mater.*, 2013, **25**, 4898–4905.

2 Y. Liu, S. Zhou, D. Tu, Z. Chen, M. Huang, H. Zhu, E. Ma and X. Chen, *J. Am. Chem. Soc.*, 2012, **134**, 15083–15090.

3. E. i. Altinoglu, T. J. Russin, J. M. Kaiser, B. M. Barth, P. C. Eklund, M. Kester and J. H. Adair, *ACS Nano*, 2008, **2**, 2075–2084.

4 L. D. Carlos, R. A. S. Ferreira, V. d. Z. Bermudez, B. Julian–Lopez and P. Escribano, *Chem. Soc. Rev.*, 2011, **40**, 536–549.

5 H. Gong, L. Cheng, J. Xiang, H. Xu, L. Feng, X. Shi and Z. Liu, *Adv. Funct. Mater.*, 2013, **23**, 6059–6067.
6 W. Zhao, H. Chen, Y. Li, L. Li, M. Lang and J. Shi, *Adv. Funct. Mater.*, 2008, **18**, 2780–2788.
7 S. Gai, C. Li, P. Yang and J. Lin, *Chem. Rev.*, 2013, **114**, 2343–2389.
8 D. Yue, W. Lu, C. Li, X. Zhang, C. Liu and Z. Wang, *Nanoscale*, 2014, **6**, 2137–2145.
9 J. Zhou, Z. Liu and F. Li, *Chem. Soc. Rev.*, 2012, **41**, 1323–1349.
10 F. Liu, Q. Zhao, H. You and Z. Wang, *Nanoscale*, 2013, **5**, 1047–1053.
11 F. Wang, D. Banerjee, Y. Liu, X. Chen and X. Liu, *Analyst*, 2010, **135**, 1839–1854.
12 K. A. Abel, J.-C. Boyer and F. C. J. M. van Veggel, *J. Am. Chem. Soc.*, 2009, **131**, 14644–14645.
13. L. Cheng, K. Yang, Y. Li, J. Chen, C. Wang, M. Shao, S.-T. Lee and Z. Liu, *Angew. Chem. Int. Ed.*, 2011, **50**, 7385–7390.
14. Z. Chen, L. Zhou, W. Bing, Z. Zhang, Z. Li, J. Ren and X. Qu, *J. Am. Chem. Soc.*, 2014, **136**, 7498–7504.
15 R. Sivakumar, F. van Veggel and M. Raudsepp, *J. Am. Chem. Soc.*, 2005, **127**, 12464–12465.
16 M. Haase and H. Schaefer, *Angew. Chem. Int. Ed.*,2011, **50**, 5808–5829.
17 Z. L. Wang, J. H. Hao, H. L. W. Chan, W. T. Wong and K. L. Wong, *Small*, 2012, **8**, 1863–1868.
18 X. He and B. Yan, *J. Mater. Chem. C*, 2013, **1**, 3910–3912.
19 K. Nguyen Tri, S. W. Kim, T. Doan Van, D.-H. Yoo, E. J. Kim and S. H. Hahn, *CrystEngComm*, 2014, **16**, 1344–1350.
20 G. Hadiko, Y. S. Han, M. Fuji and M. Takahashi, *Mater. Lett.*, 2005, **59**, 2519–2522.
21 Q. He and J. Shi, *J. Mater. Chem.*, 2011, **21**, 5845–5855.
22 Y. Zhuang, Y. Yang, G. Xiang and X. Wang, *J. Phys. Chem. C*, 2009, **113**, 10441–10445.
23 C. Zhou, Y. Zhao, T. Bian, L. Shang, H. Yu, L.-Z. Wu, C.-H. Tung and T. Zhang, *Chem. Commun.*, 2013, **49**, 9872–9874.
24 H. Schaefer, P. Ptacek, O. Zerzouf and M. Haase, *Adv. Funct. Mater.*, 2008, **18**, 2913–2918.
25 G. Wang, Q. Peng and Y. Li, *Acc. Chem. Res.*, 2011, **44**, 322–332.
26 H. X. Mai, Y. W. Zhang, R. Si, Z. G. Yan, L. D. Sun, L. P. You and C. H. Yan, *J. Am. Chem. Soc.*, 2006, **128**, 6426–6436.
27 C. Li and J. Lin, *J. Mater. Chem.*, 2010, **20**, 6831–6847.
28 F. Liu, X. He, L. Liu, H. You, H. Zhang and Z. Wang, *Biomaterials*, 2013, **34**, 5218–5225.
29 H. M. Chen, R.-S. Liu, M.-Y. Lo, S.-C. Chang, L.-D. Tsai, Y.-M. Peng and J.-F. Lee, *J. Phys. Chem. C* 2008, **112**, 7522–7526.
30 L. Tian, X. Yang, P. Lu, I. D. Williams, C. Wang, S. Ou, C. Liang and M. Wu, *Inorg. Chem.*, 2008, **47**, 5522–5524.
31 X. Liang, X. Wang, Y. Zhuang, B. Xu, S. Kuang and Y. Li, *J. Am. Chem. Soc.*, 2008, **130**, 2736–2737.
32 H. Li, Z. Bian, J. Zhu, D. Zhang, G. Li, Y. Huo, H. Li and Y. Lu, *J. Am. Chem. Soc.*, 2007, **129**, 8406–8407.
33 H. P. Liang, H. M. Zhang, J. S. Hu, Y. G. Guo, L. J. Wan and C. L. Bai, *Angew. Chem. Int. Ed.*, 2004, **43**, 1540–1543.
34 J. T. Zhang, J. F. Liu, Q. Peng, X. Wang and Y. D. Li, *Chem. Mater.*, 2006, **18**, 867–871.
35 M. Ogawa and M. Hiramine, *Cryst. Growth Des.*, 2014, **14**, 1516–1519.
36 F. Zhang, Y. Shi, X. Sun, D. Zhao and G. D. Stucky, *Chem. Mater.*, 2009, **21**, 5237–5243.
37 J. Zhuang, X. Yang, J. Fu, C. Liang, M. Wu, J. Wang and Q. Su, *Cryst. Growth Des.*, 2013, **13**, 2292–2297.
38 C. Dong and F. C. J. M. van Veggel, *Acs Nano*, 2009, **3**, 123–130.
39 Q. Lin, Q. Huang, C. Li, C. Bao, Z. Liu, F. Li and L. Zhu, *J. Am. Chem. Soc.*, 2010, **132**, 10645–10647.
40 B. Sahoo, K. S. P. Devi, R. Banerjee, T. K. Maiti, P. Pramanik and D. Dhara, *ACS Appl. Mater. Interfaces*, 2013, **5**, 3884–3893.
41 J. Nam, N. Won, H. Jin, H. Chung and S. Kim, *J. Am. Chem. Soc.*, 2009, **131**, 13639–13645.
42 W. B. Park, Y. Song, M. Pyo and K.-S. Sohn, *Opt. Lett.*, 2013, **38**, 1739–1741.
43 S.-S. Wang, W.-T. Chen, Y. Li, J. Wang, H.-S. Sheu and R.-S. Liu, *J. Am. Chem. Soc.*, 2013, **135**, 12504–12507.
44 G. Tian, Z. Gu, L. Zhou, W. Yin, X. Liu, L. Yan, S. Jin, W. Ren, G. Xing, S. Li and Y. Zhao, *Adv. Mater.*, 2012, **24**, 1226–1231.
45 X. Xie, N. Gao, R. Deng, Q. Sun, Q.-H. Xu and X. Liu, *J. Am. Chem. Soc.*, 2013, **135**, 12608–12611.
46 Y.-F. Wang, G.-Y. Liu, L.-D. Sun, J.-W. Xiao, J.-C. Zhou and C.-H. Yan, *ACS Nano*, 2013, **7**, 7200–7206.
47. S. P. Sherlock, S. M. Tabakman, L. Xie and H. Dai, *Acs Nano*, 2011, **5**, 1505–1512.
48 X.-H. Zhang, D. Zeng, L. Zhang, H. Zhu, G.-H. Jin, Z. Xie, X. Chen, J. Kang and L. Zheng, *Nanotechnology*, 2011, **22**, 185703.
49 T. Sun, A.-H. Li, C. Xu, Y.-H. Xu and R. Wang, *Opt. Laser Technol.*, 2014, **56**, 322–325.
50 X. Li, R. Wang, F. Zhang, L. Zhou, D. Shen, C. Yao and D. Zhao, *Sci. Rep.*, 2013, **3**, 3536.
51 Y. W. Zhang, X. Sun, R. Si, L. P. You and C. H. Yan, *J. Am. Chem. Soc.*, 2005, **127**, 3260–3261.
52 D. Yang, X. Kang, P. a. Ma, Y. Dai, Z. Hou, Z. Cheng, C. Li and J. Lin, *Biomaterials*, 2013, **34**, 1601–1612.
53 Y. Dai, C. Zhang, Z. Cheng, P. a. Ma, C. Li, X. Kang, D. Yang and J. Lin, *Biomaterials*, 2012, **33**, 2583–2592.
54 H.-T. Wong, M.-K. Tsang, C.-F. Chan, K.-L. Wong, B. Fei and J. Hao, *Nanoscale*, 2013, **5**, 3465–3473.
55 Z. Li and Y. Zhang, *Angew. Chem. Int. Ed.*, 2006, **45**, 7732–7735.
56 Z.-L. Wang, J. Hao, H. L. W. Chan, G.-L. Law, W.-T. Wong, K.-L. Wong, M. B. Murphy, T. Su, Z. H. Zhang and S. Q. Zeng, *Nanoscale*, 2011, **3**, 2175–2181.
57 Y. Zhong, G. Tian, Z. Gu, Y. Yang, L. Gu, Y. Zhao, Y. Ma and J. Yao, *Adv. Mater.*, 2014, **26**, 2831–2837.
58 A. Yin, Y. Zhang, L. Sun and C. Yan, *Nanoscale*, 2010, **2**, 953–959.
59 S. Heer, K. Kompe, H. U. Gudel and M. Haase, *Adv. Mater.*, 2004, **16**, 2102–2104.
60 F. Wang and X. Liu, *J. Am. Chem. Soc.*, 2008, **130**, 5642–5643.
61 X. Xie and X. Liu, *Nat. Mater.*, 2012, **11**, 842–843.
62 Y. Liu, D. Tu, H. Zhu and X. Chen, *Chem. Soc. Rev.*, 2013, **42**, 6924–6958.
63 Q. Zhang and B. Yan, *Chem. Commun.*, 2011, **47**, 5867–5869.